

# From Slices to Structures: Unsupervised 3D Reconstruction of Female Pelvic Anatomy from Freehand Transvaginal Ultrasound

Max Krähenmann, Sergio Tascon-Morales, Fabian Laumer, Julia E. Vogt, and Ece Ozkan

**Abstract**—Volumetric ultrasound has the potential to significantly improve diagnostic accuracy and clinical decision-making, yet its widespread adoption remains limited by dependence on specialized hardware and restrictive acquisition protocols. In this work, we present a novel unsupervised framework for reconstructing 3D anatomical structures from freehand 2D transvaginal ultrasound (TVS) sweeps, without requiring external tracking or learned pose estimators. Our method adapts the principles of Gaussian Splatting to the domain of ultrasound, introducing a slice-aware, differentiable rasterizer tailored to the unique physics and geometry of ultrasound imaging. We model anatomy as a collection of anisotropic 3D Gaussians and optimize their parameters directly from image-level supervision, leveraging sensorless probe motion estimation and domain-specific geometric priors. The result is a compact, flexible, and memory-efficient volumetric representation that captures anatomical detail with high spatial fidelity. This work demonstrates that accurate 3D reconstruction from 2D ultrasound images can be achieved through purely computational means, offering a scalable alternative to conventional 3D systems and enabling new opportunities for AI-assisted analysis and diagnosis.

**Index Terms**—Unsupervised 2D-to-3D reconstruction, transvaginal ultrasound, Gaussian Splatting, ultrasound rasterization

## I. INTRODUCTION

Three-dimensional (3D) ultrasound (US) imaging plays an essential role in obstetrics and gynecology, providing clinicians with a spatial context that is crucial for diagnosis, surgical planning, and treatment monitoring [1], [2]. Transvaginal ultrasound (TVS) is widely used for high-resolution imaging of pelvic organs due to its affordability, safety, and minimally invasive nature, extending 2D TVS to 3D imaging remains technically challenging. Existing 3D US systems typically rely on external tracking mechanisms or mechanically swept probes. However, while 3D ultrasound imaging is commonly performed both transabdominally and transvaginally, especially in obstetric applications such as fetal imaging, most

commercially available 3D systems are primarily designed for abdominal or general freehand use and are not specifically optimized for transvaginal applications in gynecological contexts [3], [4]. In addition to being physically cumbersome and difficult to integrate into routine clinical workflows, these systems often suffer from lower resolution compared to conventional 2D imaging. The reliance on mechanical scanning or external tracking can introduce motion artifacts, particularly in dynamic or less controlled scanning environments. Furthermore, the need for specialized hardware increases system complexity and cost, which hinder widespread adoption.

Recent advances have explored machine learning-based methods for reconstructing 3D volumes from freehand 2D ultrasound sweeps. These approaches include pose estimation using speckle correlation, deep neural networks, and self-supervised trajectory inference [5], [6], [7]. While promising in specific domains, such methods are highly dependent on the training data, sensitive to imaging artifacts, and often lack generalizability across different acquisitions or anatomical regions. Current approaches still rely on generating pose information prior to reconstruction, which introduces an additional layer of complexity [8].

In this work, we propose an alternative paradigm: an unsupervised method for 3D US reconstruction that is free from the need for any external tracking or learned pose estimation. Our method is specifically designed for the gynecological domain and operates on standard 2D TVS sweeps acquired freehand. It leverages recent advances in volumetric rendering, adapting Gaussian Splatting [9] to the constraints and physics of US imaging. Our approach uses sensorless geometric estimation of probe motion to establish spatial coherence between slices, and reconstructs anatomical structures using anisotropic Gaussian primitives optimized directly from US data.

Our method consists of three key components: (1) sensorless probe position estimation, based on sweep consistency and domain-specific geometric assumptions, (2) a volumetric representation using learned isotropic Gaussians that model anatomy with flexibility and memory efficiency, and (3) a custom CUDA-optimized differentiable rasterizer tailored to the non-optical, slice-based nature of US acquisition. Unlike voxel-based interpolation or view synthesis, Gaussian Splatting enables detailed and adaptive reconstruction without the constraints of a fixed voxel grid. Importantly, our method makes no assumptions about trajectories, requires no calibra-

J.E. Vogt and E. Ozkan share last-authorship.

This work was supported by the InnoSuisse grant 119.406 IP-LS.

M. Krähenmann is with ETH Zurich, Universitaetstrasse 6, 8092, Zurich, Switzerland (e-mail: maxkr@student.ethz.ch).

F. Laumer is with Scanvio Medical AG, Zurich, Switzerland (e-mail: fabian.laumer@scanvio.com).

S. Tascon-Morales, J. E. Vogt and E. Ozkan are with ETH Zurich, Universitaetstrasse 6, 8092, Zurich, Switzerland (e-mail: {sergio.tasconmorales, julia.vogt, ece.oezkanelsen}@inf.ethz.ch).

tion data, and does not rely on training with large datasets.

We validate our method on real-world clinical TVS data, reconstructing 3D volumes from two orthogonal freehand sweeps. Despite being unsupervised and model-free, our approach produces anatomically accurate volumes that clearly capture key structures such as the uterus and endometrium, with strong visual and spatial fidelity. Our method also demonstrates robustness under realistic acquisition conditions and shows potential for real-time performance. In summary, our contributions are:

- An unsupervised 3D reconstruction method from 2D TVS sweeps, requiring no external tracking or learned pose estimators.
- A custom volumetric framework using Gaussian Splatting, adapted for US-specific imaging physics.
- A CUDA-optimized differentiable rasterizer tailored for discrete and anisotropic slice-based rendering.

## II. RELATED WORK

2D to 3D US reconstruction has been approached using a variety of strategies. These approaches differ significantly in their reliance on external tracking hardware, training data, and assumptions about probe motion, each carrying implications for their suitability in clinical workflows, particularly in TVS.

Early freehand US systems often relied on external tracking hardware, such as electromagnetic sensors, to determine the spatial position and orientation of each 2D slice [10]. However, these systems are not suitable for TVS due to their bulk, line-of-sight limitations, and added patient discomfort [5]. To overcome these constraints, sensorless reconstruction methods were developed based on signal processing techniques. One foundational approach used speckle decorrelation, where the characteristic speckle pattern in US images was leveraged to infer probe movement [11], [12]. Despite its innovation, this method is limited by noise sensitivity and an inability to handle complex multi-axis motion, especially common in freehand TVS sweeps [13]. Spatial correlation techniques, such as normalized cross-correlation or sum-of-absolute-differences, were also explored to estimate small in-plane shifts [14]. These methods, while effective for minor linear movements, performed poorly with rotational or elevational displacement. More sophisticated approaches attempted to improve robustness through statistical models and trajectory smoothing, such as graph-based optimization constrained by speckle variation [15]. Nevertheless, these approaches remained fragile and were rarely adopted outside of research settings.

With the rise of deep learning, supervised learning methods for pose estimation gained popularity. These approaches train convolutional or recurrent neural networks to predict either inter-frame transformations or directly reconstruct 3D volumes. Early models such as [6] demonstrated that CNNs could infer relative probe motion from US frames, enabling trackerless 3D reconstruction. Later methods like DC<sup>2</sup>-Net [16] introduced contrastive and temporal losses to improve trajectory consistency across sequences. Another noteworthy model is PLPPI, which incorporates domain-specific physics constraints into the learning pipeline, enabling improved handling of out-of-plane motion [17]. However, a shared limitation

of these models is their dependency on ground truth data from tracked acquisitions for training and evaluation. In many clinical workflows—particularly for TVS—such tracking data is unavailable or infeasible to collect. Some recent works like RecON [18] explore online learning, updating models in real-time as new frames are acquired. While promising for reducing drift and latency, these methods still presuppose access to prior 3D volumes or strong priors, making them unsuitable for fully unsupervised clinical settings.

In parallel, implicit representations like Neural Radiance Fields (NeRF) [19] and subsequent developments (e.g., ImplicitVol [4]) model 3D structures as continuous functions learned by neural networks. These models offer resolution independence and are memory-efficient but require extensive training and typically rely on known camera poses—conditions not met in US. These models offer resolution independence and are memory-efficient but typically require extensive training and known camera poses—conditions that are generally not met in US unless a tracking device is present. Hybrid methods such as RapidVol [7] attempt to blend implicit and explicit approaches, using tri-planar maps refined by lightweight networks to accelerate training and inference. However, even these models typically assume access to 3D volumes for training or initialization.

Beyond motion estimation, the choice of volumetric representation plays a central role in reconstruction quality and efficiency. Traditional explicit methods such as voxel grids offer high interpretability and easy integration into existing medical imaging pipelines. However, they suffer from cubic memory growth with resolution and are thus computationally intensive for fine anatomical detail. More recently, techniques like Gaussian Splatting have emerged as a powerful alternative. Originally developed for real-time rendering in computer vision [9], Gaussian Splatting represents scenes using parameterized Gaussian primitives whose locations, shapes, and radiance are optimized to match rendered views. UltraGauss [8] adapted this to fetal US imaging by incorporating anisotropic Gaussians and integrating pose predictions from QAERTS [20]. This approach improves rendering quality but still depends on learned pose models, which hinders generalization and deployment in tracking-free environments.

In contrast to these existing approaches, our method introduces the first application of Gaussian Splatting for 3D US that is entirely unsupervised and sensorless. We eliminate the need for pose estimation models, supervision, or tracking hardware by leveraging geometric assumptions on sweep motion and optimizing isotropic Gaussian primitives directly from 2D TVS slices. This enables anatomically accurate, scalable 3D reconstruction using only standard 2D US equipment, significantly lowering the barrier to clinical deployment and advancing the capabilities of low-cost US imaging.

## III. DATASETS

To develop and evaluate our unsupervised 3D reconstruction framework, we utilize both real and synthetic TVS data. Synthetic data offers controlled conditions with ground-truth pose labels for benchmarking, while real clinical sweeps provide representative anatomical complexity and scanning variability.

### A. Synthetic Data

To support development and controlled evaluation, we construct a synthetic dataset. Starting from a 3D uterus mesh in STL format, we voxelized the model into a segmentation volume with three labels: interior (0.5), border (1), and exterior (0). Using 3D Slicer [21], slices are generated by simulating probe rotations through angular sweeps, ranging from  $-60^\circ$  to  $+60^\circ$  in sagittal and transversal directions, as shown in Fig. 1. To reflect realistic acquisition scenarios, the slices are sparsely sampled along each sweep, with a limited number of angular steps per direction, resulting in a coarse and uneven spatial coverage of the volume.

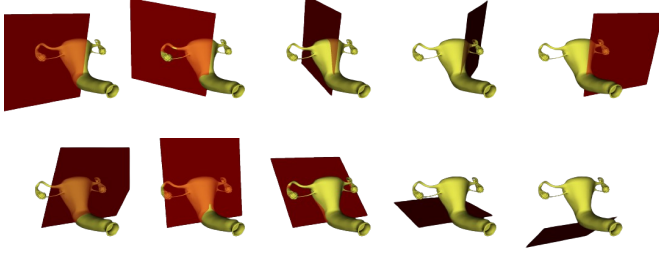


Fig. 1. *Top*: Simulated sagittal sweep. *Bottom*: Simulated transversal sweep. The image only shows some of the generated probe rotations.

Each slice is associated with a known 6D pose vector:

$$\mathbf{y} = [r_x, r_y, r_z, t_x, t_y, t_z], \quad (1)$$

where  $\mathbf{r}$  and  $\mathbf{t}$  denote Euler angles and translations with respect to a canonical coordinate system. This ground truth facilitates quantitative evaluation of slice pose and 3D reconstruction accuracy. Examples of generated frames are shown in Fig. 2 for sagittal (left) and transversal (right).

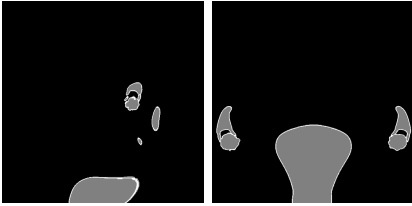


Fig. 2. Synthetic ultrasound slices generated from a simulated uterus model using a renderer. *Left*: Sagittal view showing longitudinal anatomy. *Right*: Transversal view perpendicular to the sagittal plane.

### B. Real Data

12 TVS sweeps were acquired from 6 patients (2 sweeps per patient) using a GEHC Voluson Expert 22 ultrasound machine. Table I summarizes the main parameters of the data. Each sweep represents either a sagittal or transversal view, with probe motion approximated as a smooth angular trajectory. An example image for both modalities can be seen in Fig. 3. Each patient provided written informed consent prior to participation, and all procedures adhered to strict ethical standards to ensure confidentiality and privacy. Since real data lacks tracked probe poses, we assume consistent frame intervals and smooth probe motion. We initialize the pose of each

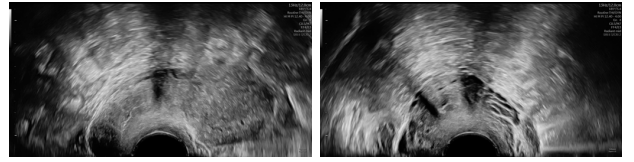


Fig. 3. Two frames sampled from the real data sweeps. On the left, a frame taken from the sagittal view. On the right, a frame taken from the transversal view.

frame using equal angular spacing. This assumption mirrors the angular sampling strategy used in generating synthetic data. Other than resizing and padding images when needed, no additional transformations or data augmentation techniques are applied, ensuring that the intrinsic properties of the images are preserved. Our method assumes (i) temporally ordered slices with approximately uniform angular spacing, and (ii) minimal tissue deformation during the sweep. These assumptions are critical for effective sensorless reconstruction, and we analyze their impact in Section IV.

## IV. UNSUPERVISED GAUSSIAN SPLATTING FOR ULTRASOUND

### A. Overview: From Gaussian Splatting to Ultrasound Imaging

Gaussian Splatting is a recent real-time rendering method that represents a 3D scene using volumetric Gaussian primitives [9]. Each Gaussian contributes to pixels in projected views based on its position, shape (covariance), opacity, and radiance. The method is differentiable and well-suited for learning-based optimization, particularly in settings where redundant multi-view image data is available (e.g., RGB images from moving cameras).

However, US imaging presents fundamental differences. Each image (or “slice”) corresponds to a narrow, planar cross-section of tissue, with limited or no overlap between neighboring slices. As a result, there is no redundancy between views to help maintain scene consistency. Additionally, the physics of US introduces directionality and discontinuities that standard perspective projection does not capture. This stands in contrast to Gaussian Splatting for optical images, where we work with projections of the scene onto a camera sensor, inherently providing depth information. Since US does not have this projection component and instead captures direct cross-sections, approaches relying on projection geometry cannot be

TABLE I  
MAIN PARAMETERS OF REAL DATA. VALUES IN PARENTHESES REPRESENT THE STANDARD DEVIATION.

Parameter	Value(s)
fps	10-20
Duration	10 seconds
Frames per sweep	100-300
Plane	sagittal / transversal
Age	38.33 (8.48)
Height [m]	1.65 (0.04)
Weight [kg]	64.53 (5.32)
Ethnicity	White/European

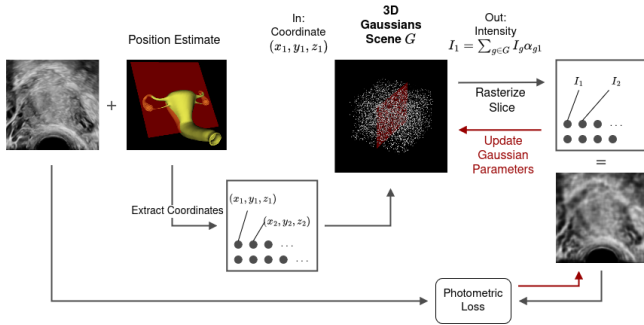


Fig. 4. Overview of our differentiable Gaussian Splatting pipeline for ultrasound volume reconstruction. A set of 3D Gaussians—each defined by a position, shape, intensity, and opacity—is rendered onto input ultrasound slice planes via a custom rasterizer. A reconstruction loss drives gradient-based optimization of all Gaussian parameters. The framework includes strategies for initialization, pruning, and performance optimization.

directly applied. Misaligned Gaussian primitives—especially in depth—can significantly affect the rendering, since each slice is extremely thin. To address these challenges, we adapt Gaussian Splatting, building a slice-aware differentiable rasterizer specifically designed for US data. Our framework accounts for the sparse and anisotropic nature of slices while retaining the strengths of the Gaussian formulation—compact, continuous scene representation and differentiability.

An overview of our method is shown in Fig. 4. We represent anatomy as a set of volumetric 3D Gaussians, which are rendered onto slice planes using a custom differentiable rasterizer. This enables end-to-end optimization of all parameters using only image-level supervision from sparse slices.

## B. Slice-Based Differentiable Rasterization

Our rasterizer computes the intensity of each pixel by aggregating contributions from a set of 3D Gaussian primitives. We begin by describing the formulation in terms of its constituent steps. Each Gaussian  $g$  is defined by a set of parameters:

- $\mu_g \in \mathbb{R}^3$ : the center of the Gaussian,
- $\Sigma_g \in \mathbb{R}^{3 \times 3}$ : the covariance matrix describing its shape and orientation. It is factored as  $\Sigma_g = (S_g R_g)^\top (S_g R_g)$ , where  $S_g$  is a diagonal scale matrix and  $R_g$  is a rotation matrix derived from a unit quaternion,
- $o_g \in [0, 1]$ : the opacity, controlling transparency,
- $I_g \in \mathbb{R}$ : the scalar intensity value associated with the Gaussian.

Each pixel  $p$  in an US slice is associated with a known 3D coordinate  $\mathbf{c}_p \in \mathbb{R}^3$ , obtained via slice pose and pixel location. For each Gaussian  $g$ , we compute the offset vector from the Gaussian center to the pixel coordinate:

$$\mathbf{d}_{gp} = \mathbf{c}_p - \mu_g, \quad (2)$$

This displacement indicates how far and in which direction pixel  $p$  lies from the Gaussian center. We use the Mahalanobis distance to compute how “close” the pixel is to the Gaussian in the metric induced by the covariance:

$$e_{gp} = -\frac{1}{2} \mathbf{d}_{gp}^\top \Sigma_g^{-1} \mathbf{d}_{gp}. \quad (3)$$

This term governs the spatial falloff of the Gaussian’s influence. A higher value of  $e_{gp}$  (closer to 0) means greater contribution. The influence of Gaussian  $g$  at pixel  $p$  is then:

$$\alpha_{gp} = o_g \exp(e_{gp}), \quad (4)$$

where  $o_g$  scales the exponential according to the visibility (opacity) of the Gaussian. The final intensity  $I_p$  at pixel  $p$  is computed as a weighted sum of intensities from all Gaussians:

$$I_p = \sum_g \alpha_{gp} I_g. \quad (5)$$

This formulation defines each pixel as the sum of soft and spatially-varying influences from 3D Gaussians. By using Gaussian functions instead of hard surface projections, the method can represent continuous, soft-tissue-like structures and remains differentiable. It is especially well-suited for sparse and anisotropic data such as US slices, where direct projection is unreliable and information across slices is limited.

## C. Gradient-Based Optimization

To enable end-to-end training of our differentiable rasterizer, we must compute gradients of the loss  $L$  with respect to all learnable parameters of each Gaussian primitive. These include the intensity  $I_g$ , opacity  $o_g$ , mean position  $\mu_g$ , and covariance  $\Sigma_g$  (parameterized via scale and rotation). Unlike standard neural network layers, our rasterizer is implemented as a custom CUDA kernel for performance reasons, which precludes the use of automatic differentiation frameworks such as PyTorch’s autograd. Therefore, we manually derive analytic gradients for all parameters using the chain rule and matrix calculus. The key components of this gradient-based optimization pipeline are as follows:

- **Intensity and opacity gradients**  $\left(\frac{\partial L}{\partial I_g}, \frac{\partial L}{\partial o_g}\right)$ : These are computed directly from the contribution term  $\alpha_{gp} = o_g \exp(e_{gp})$ , where each Gaussian’s influence on a pixel is determined by how close it is and how opaque it is.
- **Mean position gradients**  $\left(\frac{\partial L}{\partial \mu_g}\right)$ : The spatial location of the Gaussian strongly affects the rendering. We compute how shifting the Gaussian in 3D space changes its contribution to all nearby pixels.
- **Covariance gradients**  $\left(\frac{\partial L}{\partial \Sigma_g}\right)$ : The shape and spread of the Gaussian control its spatial footprint. We derive the gradient of the Mahalanobis exponent and backpropagate through the decomposition  $\Sigma_g = (S_g R_g)^\top (S_g R_g)$ .
- **Scale and rotation gradients**: Since we do not directly optimize  $\Sigma_g$ , we propagate the covariance gradient to scale and rotation components. The scale is assumed diagonal, while rotation is parameterized via unit quaternions.
- **Quaternion backpropagation**: We compute gradients through the rotation matrix  $R(q_g)$  and its analytical Jacobian with respect to the quaternion  $q_g$ . We also account for the normalization of quaternions to ensure they remain on the unit sphere.

This modular decomposition of the backward pass ensures numerical stability, supports high-performance GPU execu-

tion, and allows all Gaussian parameters to be learned efficiently during training. For full derivations, see App. A.

#### D. Parameter Initialization

Effective initialization of Gaussian parameters is crucial to ensure stable and efficient optimization. This is particularly important because the contribution of each Gaussian to the rendered image, thus, the magnitude of its gradient updates—depends multiplicatively on both its intensity  $I_g$  and opacity  $o_g$ . If these parameters are poorly initialized (e.g., near zero), the Gaussian becomes effectively invisible and receives negligible gradient updates, rendering it “inactive” from the outset. If initialized randomly, we could potentially run into such issues; the following values were found to work well empirically for our setting:

- For moderate initial opacity,  $o_g = \sigma(1.0) \approx 0.73$ ,
- For mid-range intensity,  $I_g = 0.5$ ,
- For moderate spatial extent,  $\mathbf{s}_g = \exp([0.5, 0.5, 0.5])^\top \approx [1.65, 1.65, 1.65]^\top$
- For identity rotation,  $\mathbf{q}_g = [1, 0, 0, 0]^\top$ .

This choice of initialization ensures that each Gaussian has a non-negligible influence on the rendered slice at the start of training, gradients with respect to spatial and shape parameters are not suppressed, and training begins from a smooth, isotropic configuration, avoiding early instability from sharp or ill-posed Gaussians. Unlike opacity and intensity, the mean position  $\mu_g \in \mathbb{R}^3$  is highly sensitive to initialization. Gaussians must be spatially close to the slices they are meant to influence; otherwise, their contribution to the rendered image (and thus their gradient signal) is exponentially suppressed via the term  $\exp(e_{gp})$ . In practice, we found that poor initialization of  $\mu_g$  leads to Gaussians becoming permanently inactive before they can migrate toward meaningful regions. We consider two strategies for initializing  $\mu_g$ :

- *On-slice initialization*: When the spatial positions and orientations of the US slices are known (e.g., via a tracking system), we distribute the Gaussian centers uniformly across the slices. This ensures that Gaussians are positioned exactly where they are needed from the start, resulting in strong gradient signals and faster convergence.
- *Uniform sampling in a bounding volume*: In cases where slice poses are unknown or unreliable, we sample Gaussian centers uniformly from a predefined 3D bounding box that encloses the volume of interest.

While this strategy is more agnostic and flexible, it often requires additional optimization time for Gaussians to migrate toward active regions. The full mathematical formulation and a visual comparison of both methods is provided in App. B.

#### E. Inactive Gaussians and Density Control

During training, certain Gaussians may become effectively “inactive”—typically those initialized in regions of the volume that are consistently dark or far from any informative US data. These Gaussians tend to receive low gradient signals, leading to rapid decay of their opacity  $o_g$  and intensity  $I_g$  toward

zero. Once these values are sufficiently small, the Gaussian’s contribution to the image becomes negligible, which in turn suppresses all subsequent gradient updates to its position, shape, and rotation. In effect, these Gaussians are permanently frozen in an uninfluential state.

Such inactive Gaussians waste computational resources during both the forward and backward passes. To mitigate this, we incorporate a lightweight yet effective density control mechanism that periodically removes such Gaussians and replaces them with new ones better positioned to contribute meaningfully.

We define a simple but effective scalar activity metric:

$$m_g = |I_g \cdot o_g|$$

Gaussians for which  $m_g < \epsilon$  (where  $\epsilon$  is a small predefined threshold) are considered inactive. These are removed from the parameter set every  $N$  optimization steps. This process is efficient to implement and avoids the overhead of evaluating gradient norms or rendering error sensitivity for Gaussians.

To maintain a constant number of Gaussians in the scene, we reintroduce new ones to replace those pruned. Rather than randomly sampling across the entire volume (which could repeat the problem), we restrict the new means  $\mu_g$  to be sampled uniformly within the current bounding box of active Gaussians:

$$\mu_{\text{new}} \sim \mathcal{U}[\mu_{\text{min}}, \mu_{\text{max}}]$$

This simple heuristic leverages the existing distribution of active Gaussians to guide new candidates toward potentially informative regions, without requiring a full analysis of image-space reconstruction error. Other parameters are reset to default values as described in Sec. IV-D.

As a complementary strategy, we apply a non-uniform learning rate schedule where the Gaussian means  $\mu_g$  are updated more aggressively than other parameters (e.g., opacity, intensity, and rotation). The motivation is to allow Gaussians to quickly migrate toward regions where they influence the rendered image before their visibility is “shut off” by the optimizer. In more extreme variants, we temporarily freeze non-positional parameters entirely during early training epochs. This prevents premature deactivation and leads to more effective exploration of the volume.

Both the pruning–reinitialization mechanism and learning rate scheduling are essential for maintaining a healthy and responsive population of Gaussians during training. Full details are provided in App. C.

#### F. Practical Considerations for Implementation

To make training tractable at scale, we apply a series of CUDA-level optimizations across both the forward and backward passes of the differentiable rasterizer. In particular, we precompute invariant quantities such as inverse covariance matrices ( $\Sigma_g^{-1}$ ), which can then be reused across all affected pixels. We also adopt shared memory tiling, where Gaussian parameters are loaded once per tile and reused by all threads in a block, thereby minimizing global memory traffic. Further efficiency is gained through symmetry-aware matrix handling,

which exploits the symmetric structure of covariance matrices to reduce both memory usage and compute overhead, and through matrix-free computation strategies that replace expensive general-purpose matrix operations with lightweight element-wise arithmetic. Finally, compiler-level tuning, including the use of aggressive optimization flags and fast math approximations, further accelerates execution. Together, these optimizations improve training throughput by an order of magnitude compared to a naive implementation and are critical for scaling to tens of thousands of Gaussians in high-resolution 3D volumes. Detailed descriptions and performance results are provided in App. E.

## V. EXPERIMENTS AND RESULTS

### A. Experimental Setup

We conducted initial experiments to identify optimal default parameters for training. Image resolution and batch size were selected to balance reconstruction quality with computational constraints, particularly GPU memory. The remaining settings were empirically tuned to ensure high-fidelity outputs across diverse inputs. Unless otherwise specified, all subsequent experiments use the configuration detailed in Table II. The selection of specific values is explained in more detail in Sec. V-B. We divide the experiments into optimizations (Sec. V-B) and reconstruction quality (Sec. V-C). To comprehensively evaluate model performance, we report standard image similarity metrics: Structural Similarity Index Measure (SSIM), Mean Absolute Error (MAE), Mean Squared Error (MSE), Peak Signal-to-Noise Ratio (PSNR), and Normalized Cross-Correlation (NCC), using their conventional formulations.

### B. Optimizations

As outlined in Sec. IV, applying Gaussian Splatting to TVS introduces specific difficulties due to the shift from a pinhole camera model to the physical characteristics of US image formation. Key issues include identifying a suitable loss function, defining effective initialization strategies, and addressing common problems such as inactive Gaussians. In the following, we detail the solutions adopted to address these.

TABLE II  
DEFAULT CONFIGURATION FOR ALL EXPERIMENTS.

Category	Value
Input resolution	256×256 px
Slices per sweep	100
Number of Gaussians	120 per slice ( $\approx$ 12k)
Loss	Hybrid L1 (80%) + SSIM (20%) Means:0.20,
Learning rates	Opacity:0.03, Scale:0.01, Intensity:0.008
Batch size	32 slices
Epochs	60

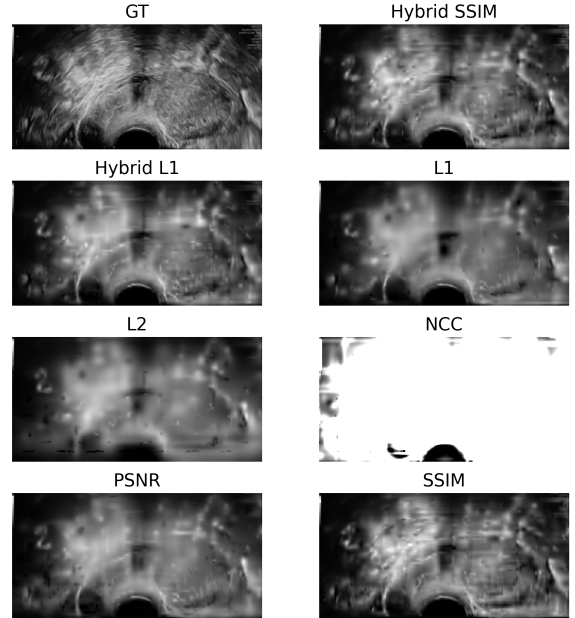


Fig. 5. Images rendered using commonly used loss functions, such as L1, L2, SSIM, PSNR, and NCC. We also tested hybrid configurations, referred to as “Hybrid L1” (80% L1, 20% SSIM) and “Hybrid SSIM” (20% L1, 80% SSIM).

1) *Training Objective*: Selecting an appropriate loss function is essential, as it shapes the optimization trajectory and affects both the accuracy and perceptual quality of the final reconstruction. Each loss emphasizes different aspects of fidelity—for instance, local pixel differences or broader structural consistency. To determine the most effective objective for US image reconstruction within our framework, we assessed a range of commonly used losses: L1, L2, SSIM, PSNR, and NCC. We also tested hybrid configurations, referred to as “Hybrid L1” (80% L1, 20% SSIM) and “Hybrid SSIM” (20% L1, 80% SSIM). To ensure a fair comparison, we first determine the optimal learning rate for each objective through preliminary experiments without advanced optimizations. After determining the optimal rates, we trained the model under each loss configuration and assessed performance across a broad set of evaluation metrics. A quantitative comparison of the results is provided in Table III. Some qualitative results are in Fig. 5. Showing robustness in most metrics, the hybrid L1 loss is selected for further optimizations and experiments.

TABLE III  
METRIC VALUES FOR EVALUATED LOSS FUNCTIONS. HYBRID L1 DENOTES 80% L1 AND 20% SSIM, WHEREAS HYBRID SSIM INDICATES 20% L1 AND 80% SSIM.

Loss Type	L1 ( $\downarrow$ )	L2 ( $\downarrow$ )	SSIM ( $\uparrow$ )	PSNR ( $\uparrow$ )	NCC ( $\uparrow$ )
Hybrid SSIM	0.0192	<b>0.0016</b>	0.8663	27.86	0.9791
Hybrid L1	<b>0.0188</b>	<b>0.0016</b>	0.8528	<b>28.07</b>	<b>0.9799</b>
L1	0.0198	0.0017	0.8197	27.72	0.9782
L2	0.0245	0.0023	0.7651	26.41	0.9699
NCC	3.4030	33.7651	0.4314	-15.28	0.9762
PSNR	0.0210	<b>0.0016</b>	0.8048	27.88	0.9792
SSIM	0.0198	0.0017	<b>0.8695</b>	27.61	0.9792

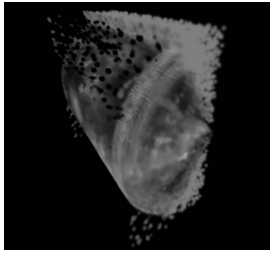


Fig. 6. Example of a 3D view scene after uniform random initialization of means.

## 2) Results of Optimization Techniques:

a) *Gaussian Mean initialization:* To evaluate the suitability of each of the initialization approaches described in Sec. IV-D, we run experiments and report the L1 and SSIM for each case, as shown in Table IV. Fig. 6 shows an example of the resulting scene obtained through uniform random initialization.

TABLE IV

L1 AND SSIM METRICS ON RUNS WITH DIFFERENT INITIALIZATION FOR SAGITTAL-ONLY, TRANSVERSAL-ONLY AND SAGITTAL & TRANSVERSAL VIEW OPTIMIZATION. NUMBER OF GAUSSIANS: 12K

Group	Init. method	L1 (↓)	SSIM (↑)
Sagittal	Random	0.0067	0.9610
	On-Slice	0.0055	0.9694
	diff.	<b>0.0012</b>	<b>0.0084</b>
Transversal	Random	0.0047	0.9717
	On-Slice	0.0037	0.9783
	diff.	<b>0.0010</b>	<b>0.0066</b>
Both	Random	0.0060	0.9655
	On-Slice	0.0054	0.9697
	diff.	<b>0.0006</b>	<b>0.0042</b>

Table IV shows that on-slice initialization yields slightly better results, and is therefore chosen as the default mean initialization method

b) *Number of Gaussians:* The total number of Gaussian primitives used to represent the volume is a key hyperparameter that directly influences both reconstruction quality and computational cost. Increasing this number provides the model with more flexibility to capture fine anatomical details, potentially enhancing reconstruction fidelity. However, this improvement comes with a higher memory footprint and significantly longer training times.

To explore this trade-off, we systematically evaluated the method’s performance by varying the number of Gaussians on a fixed set of US slices (specifically, real data sweeps). We monitored reconstruction quality metric alongside the total training time, as shown in Fig. 7. As expected, a higher number of Gaussians generally leads to improved reconstruction quality, reflected in lower L1 loss and higher SSIM scores. At the same time, training time increases substantially due to the added computational burden per iteration.

For the tested 256x256 resolution images, the results suggest an optimal range between approximately 60,000 Gaussians (about 278 per slice in the test setup) and 100,000 Gaussians (about 463 per slice), which appears to strike a good balance between reconstruction quality and computational efficiency.

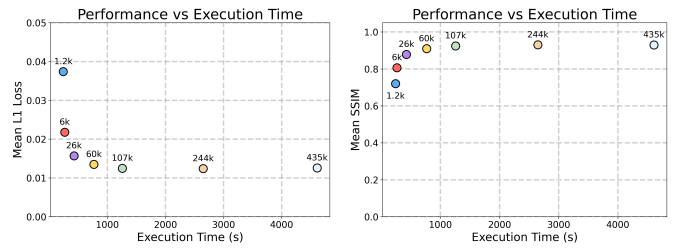


Fig. 7. L1 Loss and SSIM vs. training time for different numbers of Gaussians representing the scene.

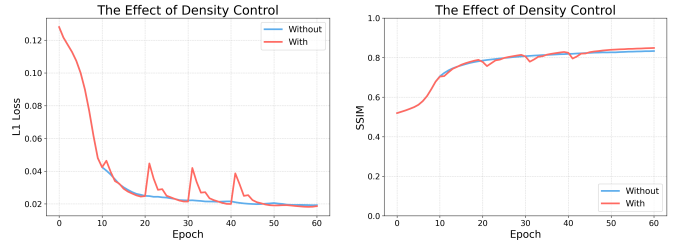


Fig. 8. Training performance with (red) and without (blue) density control, compared to the baseline using default learning rates. The spikes in the red L1 curve mark the moments when density control was applied.

Beyond roughly 100,000 Gaussians, the gains in L1 and SSIM begin to plateau, indicating diminishing returns, while the execution time continues to rise significantly. To strike a good balance between performance and execution time during experiments, we use approximately 12k Gaussians.

c) *Inactive Gaussians:* As described before, inactive Gaussians can limit the effect of a large number of primitives on the final reconstruction. We now present the results for both parameter-specific learning rates and density control.

**Parameter-specific Learning Rates:** We perform an exhaustive parameter search, obtaining the results shown in Table II. A more comprehensive analysis and specific results can be found in App. C.

**Density Control:** We apply reinitialization of Gaussians with spatial awareness, as described in Sec. IV-E, using different thresholds for pruning ( $m_g = |I_g o_g|$  values of 0.2, 0.1, 0.05, and 0.01) and tested several schedules for when to apply the removal and addition steps. The best results were obtained using a threshold of 0.05 and applying density control every 10 epochs, starting at epoch 10 and continuing until epoch 50 (specifically at epochs 10, 20, 30, and 40, given the 60-epoch training setup).

Fig. 8 shows how this method impacted training compared to the baseline without mitigation. In the L1 loss plot, the red line (“With” density control) shows spikes after each control step, caused by abrupt changes in the set of Gaussians. The loss then stabilizes, and by the end of training, both L1 and SSIM slightly outperform the baseline without density control. Fig. 9 shows the intensity, opacity, and scale distributions for the baseline (no mitigation of inactive Gaussians) and for the two proposed techniques. Notably, intensity values can be negative, allowing the model to offset overly bright areas by subtracting signal during composition. Without mitigation, distributions collapse into consistent patterns: intensity clusters

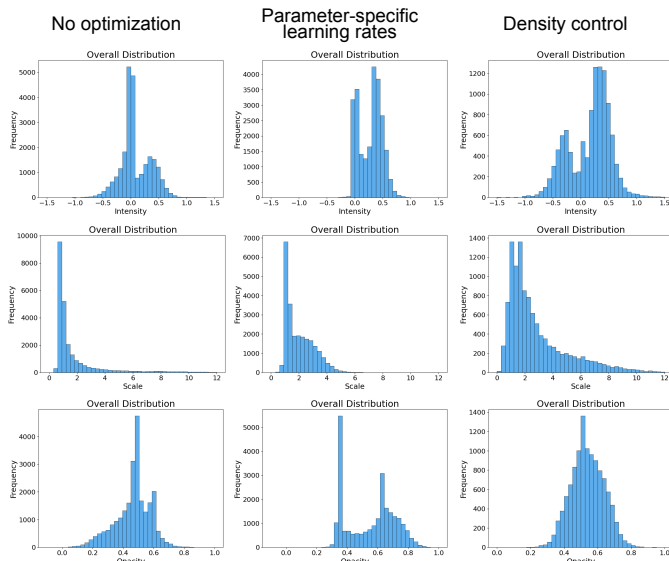


Fig. 9. Parameter distributions for no mitigation of inactive Gaussians (left), parameter-specific learning rates (middle) and density control (right).

around zero, opacities shift lower, and scales often fall below the initial 1.65, reducing each primitive’s spatial impact. In contrast, both parameter-specific learning rates and density control yield broader distributions.

Finally, when combining the two presented techniques to handle inactive Gaussians, we did not observe significant improvement over using them separately. For this reason, we adopt parameter-specific learning rates as the default technique for Gaussian deactivation in our approach.

### C. Reconstruction Quality

1) *View-Specific Reconstructions on Synthetic Data*: Based on insights gained from earlier experiments, we now evaluate the reconstruction performance of our method more closely. We begin with synthetic data, using the following setup, number of epochs set to 60, image resolution is  $256 \times 256$  pixels, number of Gaussians per slice is 276, and total number of slices is 100. With this configuration, training on sagittal and transversal sweeps took about 5 minutes each. The resulting L1 losses were 0.0049 for sagittal and 0.0034 for transversal views, with SSIM scores of 0.972 and 0.980, respectively. Fig. 10 shows the corresponding reconstructions. We observed cone-shaped artifacts when using models trained on one view to reconstruct the other. These are caused by the angle distribution of slices, which span from  $-60^\circ$  to  $60^\circ$  around their respective axes. Visually, the reconstructions are quite faithful, although small inaccuracies appear near the edges, likely due to abrupt intensity transitions in the ground truth masks. Since the synthetic data represents segmentation masks, generating 3D reconstructions is straightforward. Fig. 11 displays the 3D models reconstructed from sagittal-only, transversal-only, and combined sweeps. Combining both views yields the most complete result, but even a single sweep captures a good amount of structural information.

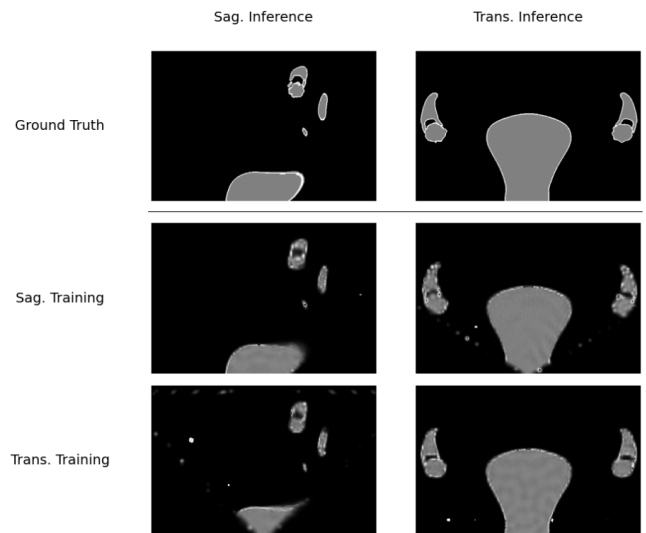


Fig. 10. Reconstruction results for sagittal and transversal sweeps. The top row shows results from sagittal training, the middle row from transversal training, and the bottom row shows the ground truth.

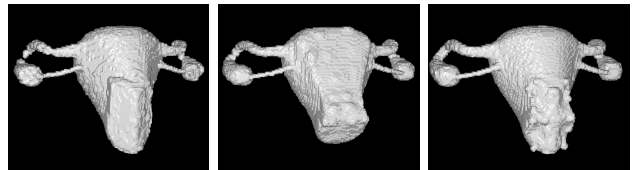


Fig. 11. 3D reconstructions using different training settings. Left: sagittal only. Middle: transversal only. Right: both sagittal and transversal.

2) *Cross-View Generalization on Real Data*: Working with real US data introduces additional challenges, particularly the lack of clear segmentation masks for structures like the uterus. As a result, we evaluate reconstruction quality by testing cross-view generalization. Fig. 12 shows that even when training is done on just one view (sagittal or transversal), the model performs well when tested on the orthogonal view. It also handles difficult regions, such as areas obscured by fluid, with surprising accuracy, which suggests good generalization. Although the model captures anatomical features well, there are alignment issues between sagittal and transversal reconstructions. This complicates training with both views simultaneously. Addressing this misalignment could significantly improve results, as confirmed by the combined-view experiments on synthetic data, where ground truth positions are known. Proper integration of both views may also help estimate slice positions more accurately, potentially moving beyond the simplified assumption of evenly spaced angles. In summary, the method demonstrates strong potential for reconstructing consistent and anatomically meaningful 3D representations from US sweeps.

3) *Effect of Slice Density*: We also analyze the impact of slice density and Gaussian count. The number of slices acquired during a sweep significantly affects reconstruction quality. We systematically varied slice density—from 10 to 200 slices—to assess how it influences our model’s performance. As shown in Fig. 13, reconstructions with very few slices (10–25) are blurry and lack anatomical detail,

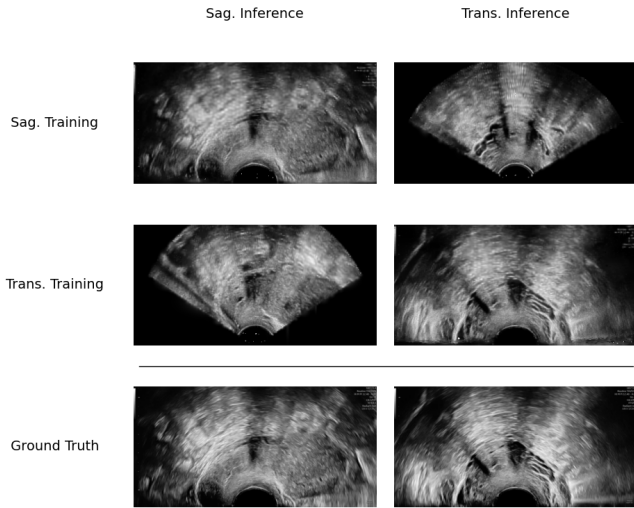


Fig. 12. Reconstructions from real data. Top: trained on sagittal view. Middle: trained on transversal view. Bottom: ground truth for comparison.

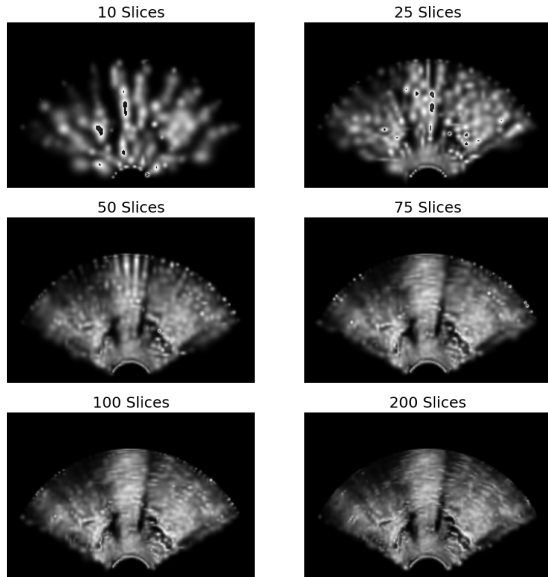


Fig. 13. Reconstruction results for different amounts of slices.

while quality improves substantially with 50 or more slices. Beyond 100 slices, gains diminish, suggesting that ultra-dense sampling offers limited additional benefit. Quantitative trends in Fig. 14 confirm this: higher slice counts result in lower L1 loss and higher SSIM, and they also accelerate convergence. Conversely, sparse setups plateau at lower fidelity and slower training. Our Gaussian primitives naturally compensate for moderate sparsity by expanding spatial support across neighboring slices. However, this ability is limited when data is extremely sparse, leading to smooth, under-detailed outputs. In contrast, denser setups allow Gaussians to reinforce structural coherence through natural overlap across slices.

4) *Effect of Gaussian Count per Slice*: To decouple the effects of slice count and Gaussian density, we fixed the total number of Gaussians ( $\approx 55,000$ ) by using an on-slice initialization assuming 200 slices, but trained the model using

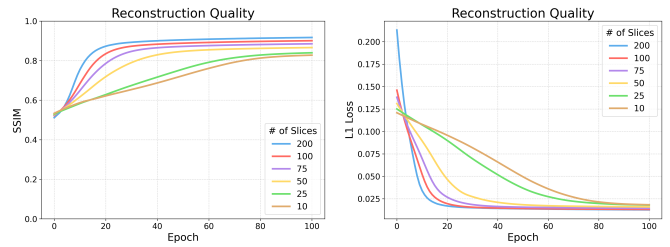


Fig. 14. L1 Loss and SSIM across epochs for different numbers of slices, same number of per-slice Gaussians.

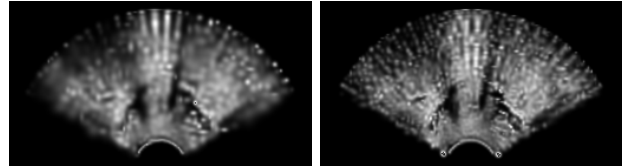


Fig. 15. Slices generated from a sagittal sweep supervised with 50 frames. Left: 13,000 Gaussians; Right: 55,000 Gaussians.

supervision from only 50 slices. This approach was compared to a baseline where both the initialization and training used 50 slices, resulting in fewer Gaussians ( $\approx 13,000$ ). As shown in Fig. 15, the higher-density setup significantly improved reconstruction quality: SSIM increased from 0.866 to 0.9276, and L1 loss decreased from 0.0159 to 0.0111. The trade-off was a 74% increase in training time. These results suggest that increasing the number of Gaussians, even if many are not initialized on the supervised slices, can compensate for sparse supervision, albeit at a higher computational cost.

#### D. Rendering Speed

Finally, we evaluate the rendering performance by measuring the average frame rate under varying scene complexities. Specifically, we benchmark scenes containing different numbers of Gaussians to assess how the rendering speed scales with model size. The results, summarized in Table V, provide a quantitative comparison across these settings.

TABLE V  
RENDERING SPEED DIFFERENT NUMBER OF GAUSSIAN PRIMITIVES, FOR 10,000 ITERATIONS.

# Gaussians	Sweep type	Mean speed [ms]	FPS
11,216	Transversal	$4.358 \pm 0.040$	229.47
	Sagittal	$4.397 \pm 0.031$	227.40
48,032	Transversal	$18.142 \pm 17.481$	55.12
	Sagittal	$18.182 \pm 17.613$	55.00

## VI. DISCUSSION

Our experiments highlight the sensitivity of the method to initialization. Gaussians placed near actual data slices converged faster and contributed more effectively to the final reconstruction, while randomly initialized primitives were often slow to optimize or entirely deactivated. Assigning higher learning rates to the mean parameters, compared to

opacity or scale, helped reduce early deactivation and encouraged convergence. Slice density was another important factor influencing performance. Denser sweeps led to higher-quality reconstructions, with fewer gaps and artifacts. Although adding more Gaussians can partially compensate for sparse data, this increases computational cost. This trade-off between reconstruction fidelity, data acquisition effort, and runtime is important to consider for clinical deployment. The method also demonstrated promising generalization across orthogonal sweep directions. Volumes trained on sagittal sweeps could generalize well to transversal inputs and vice versa. However, combining multiple views simultaneously remains a challenge, particularly due to the need for accurate alignment. Our method does not currently perform registration, which can lead to visible inconsistencies when merging sweeps.

**Practical Limitations.** Our method’s reliance on temporally ordered slices with uniform angular spacing makes it highly effective for smooth, stable acquisitions but also introduces key limitations. The reconstruction quality is sensitive to irregular motion, patient movement, or rapid changes in probe orientation, as these actions disrupt the assumed input structure. Even with CUDA acceleration, the method remains computationally intensive. Near-real-time performance may be achievable with further optimization, but current runtimes and memory demands are high, especially for large numbers of Gaussians or high-resolution data. Finally, while we demonstrated feasibility using both synthetic and real datasets, broader clinical validation is needed. Differences in patient anatomy, imaging conditions, and probe operators were not extensively studied, and generalizing to these variables will be important before the method can be adopted in practice.

**Clinical Potential.** Despite these limitations, the method shows potential for improving clinical US workflows. During TVS examination the ability to generate accurate 3D reconstructions from freehand sweeps could support better visualization and localization of subtle anatomical abnormalities and enhance surgical planing. Additionally, real-time feedback during scanning could guide clinicians in covering relevant regions more thoroughly, potentially reducing missed findings making scanning less operator dependent.. The synthetic dataset and evaluation pipeline developed as part of this work may also serve as a foundation for future studies, offering reproducible benchmarks for US reconstruction research.

## VII. CONCLUSION

We have introduced a novel, unsupervised framework for reconstructing 3D anatomical volumes from freehand 2D transvaginal US sweeps, without requiring external tracking, ground truth trajectories, or pose supervision. By adapting Gaussian Splatting to the specific physics and geometry of US imaging, and designing a custom differentiable rasterizer, our method enables accurate volumetric reconstruction from sparse, uncalibrated slice data. Through extensive experiments on both synthetic and real-world datasets, we demonstrated that the approach can achieve high-fidelity reconstructions, generalizes well across sweep orientations, and remains robust to various acquisition conditions. We showed that initializa-

tion, slice density, and the number of Gaussians are critical factors influencing performance, and proposed effective strategies for optimizing these parameters, including density control and parameter-specific learning rates. While challenges remain—particularly in handling multi-view alignment and achieving real-time performance—the results suggest strong potential for clinical deployment. Our method offers a scalable, hardware-free alternative to conventional 3D US systems and provides a foundation for future research in data-driven, volumetric reconstruction and AI-assisted gynecological imaging.

## REFERENCES

- [1] J. Alcazar, “Three-dimensional ultrasound in gynecology: Current status and future perspectives,” *Current Women’s Health Reviews*, 2005.
- [2] J. A. Jensen, “Medical ultrasound imaging,” *Progress in Biophysics and Molecular Biology*, 2007.
- [3] C. Apirakviriyaa, T. Rungruxsivorn, V. Phupong, and W. Wisawasukmongchol, “Diagnostic accuracy of 3D-transvaginal ultrasound in detecting uterine cavity abnormalities in infertile patients as compared with hysteroscopy,” *Eur J Obstet Gynecol Reprod Biol*, 2016.
- [4] P.-H. Yeung, L. Hesse, M. Aliasi, M. Haak, t. I.-s. Consortium, W. Xie, and A. I. L. Namburete, “Implicitvol: Sensorless 3D ultrasound reconstruction with deep implicit representation,” 2021.
- [5] C. Peng, Q. Cai, M. Chen, and X. Jiang, “Recent advances in tracking devices for biomedical ultrasound imaging applications,” *Micromachines*, 2022.
- [6] R. Prevost, M. Salehi, S. Jagoda, N. Kumar, J. Sprung, A. Ladikos, R. Bauer, O. Zettinig, and W. Wein, “3D freehand ultrasound without external tracking using deep learning,” *Med Image Anal*, 2018.
- [7] M. C. Eid, P.-H. Yeung, M. K. Wyburd, J. F. Henriques, and A. I. L. Namburete, “Rapidvol: Rapid reconstruction of 3D ultrasound volumes from sensorless 2D scans,” 2024.
- [8] M. C. Eid, A. I. L. Namburete, and J. F. Henriques, “UltraGauss: Ultrafast gaussian reconstruction of 3D ultrasound volumes,” 2025.
- [9] B. Kerbl, G. Kopanas, T. Leimkühler, and G. Drettakis, “3D gaussian splatting for real-time radiance field rendering,” 2023.
- [10] T. Wen, Q. Zhu, W. Qin, L. Li, F. Yang, Y. Xie, and J. Gu, “An accurate and effective fmm-based approach for freehand 3D ultrasound reconstruction,” *Biomed Signal Process Control*, 2013.
- [11] J.-F. Chen, J. B. Fowlkes, P. L. Carson, and J. M. Rubin, “Determination of scan-plane motion using speckle decorrelation: Theoretical considerations and initial test,” *Int J Imaging Syst Technol*, 1997.
- [12] A. H. Gee, R. James Housden, P. Hassenpflug, G. M. Treece, and R. W. Prager, “Sensorless freehand 3D ultrasound in real tissue: Speckle decorrelation without fully developed speckle,” *Med Image Anal*, 2006.
- [13] P.-C. Li, C.-Y. Li, and W.-C. Yeh, “Tissue motion and elevational speckle decorrelation in freehand 3D ultrasound,” *Ultrasonic Imaging*, 2002.
- [14] A. D. Gilliam, J. A. Hossack, and S. T. Acton, “Freehand 3D ultrasound volume reconstruction via sub-pixel phase correlation,” in *Int Conf on Image Proc*, 2006.
- [15] L. Tetreil, H. Chebrek, and C. Laporte, *Learning for Graph-Based Sensorless Freehand 3D Ultrasound*. 2016.
- [16] H. Guo, H. Chao, S. Xu, B. J. Wood, J. Wang, and P. Yan, “Ultrasound volume reconstruction from freehand scans without tracking,” *IEEE Trans on Biomed Eng*, 2023.
- [17] Y. Dou, F. Mu, Y. Li, and T. Varghese, “Sensorless end-to-end freehand 3-D ultrasound reconstruction with physics-guided deep learning,” *IEEE Trans Ultrason Ferroelectr Freq Control*, 2024.
- [18] M. Luo, X. Yang, H. Wang, H. Dou, X. Hu, Y. Huang, N. Ravikumar, S. Xu, Y. Zhang, Y. Xiong, W. Xue, A. F. Frangi, D. Ni, and L. Sun, “RecON: Online learning for sensorless freehand 3D ultrasound reconstruction,” *Med Image Anal*, 2023.
- [19] B. Mildenhall, P. P. Srinivasan, M. Tancik, J. T. Barron, R. Ramamoorthi, and R. Ng, “NeRF: Representing scenes as neural radiance fields for view synthesis,” 2020.
- [20] J. Ramesh, N. Dinsdale, P.-H. Yeung, and A. I. L. Namburete, *Geometric Transformation Uncertainty for Improving 3D Fetal Brain Pose Prediction from Freehand 2D Ultrasound Videos*. 2024.
- [21] A. Fedorov, R. Beichel, J. Kalpathy-Cramer, J. Finet, J.-C. Fillion-Robin, S. Pujol, C. Bauer, D. Jennings, F. Fennessy, M. Sonka, J. Buatti, S. Aylward, J. V. Miller, S. Pieper, and R. Kikinis, “3D slicer as an image computing platform for the quantitative imaging network,” *Magnetic Resonance Imaging*, 2012.

## APPENDIX

## A. Gradient Derivations

This appendix provides the detailed derivations required for manually implementing the backward pass of the differentiable rasterizer. Since the forward pass is implemented using custom CUDA kernels, we cannot rely on autograd engines and must explicitly compute partial derivatives for each Gaussian parameter.

1) *Notation Recap*: For each pixel  $p$  at coordinate  $\mathbf{c}_p \in \mathbb{R}^3$  and each Gaussian  $g$ , we define:

$$\begin{aligned}\mathbf{d}_{gp} &= \mathbf{c}_p - \mu_g, \\ e_{gp} &= -\frac{1}{2} \mathbf{d}_{gp}^\top \Sigma_g^{-1} \mathbf{d}_{gp}, \\ \alpha_{gp} &= o_g \exp(e_{gp}), \\ I_p &= \sum_g \alpha_{gp} I_g\end{aligned}$$

The loss function  $L$  depends on rendered intensities  $I_p$ , and we are given  $\frac{\partial L}{\partial I_p}$  from upstream layers.

2) *Gradient w.r.t. Gaussian Intensity  $I_g$* : Since  $I_p = \sum_g \alpha_{gp} I_g$ , differentiating w.r.t.  $I_g$  gives:

$$\begin{aligned}\frac{\partial I_p}{\partial I_g} &= \alpha_{gp} \\ \Rightarrow \frac{\partial L}{\partial I_g} &= \sum_p \frac{\partial L}{\partial I_p} \frac{\partial I_p}{\partial I_g} = \sum_p \frac{\partial L}{\partial I_p} \alpha_{gp}\end{aligned}$$

3) *Gradient w.r.t. Opacity  $o_g$* : From  $\alpha_{gp} = o_g \exp(e_{gp})$ , we get:

$$\begin{aligned}\frac{\partial \alpha_{gp}}{\partial o_g} &= \exp(e_{gp}) \\ \Rightarrow \frac{\partial L}{\partial o_g} &= \sum_p \frac{\partial L}{\partial I_p} I_g \frac{\partial \alpha_{gp}}{\partial o_g} = \sum_p I_g \frac{\partial L}{\partial I_p} \exp(e_{gp})\end{aligned}$$

4) *Gradient w.r.t. Mean  $\mu_g$* : We use:

$$\frac{\partial e_{gp}}{\partial \mathbf{d}_{gp}} = -\Sigma_g^{-1} \mathbf{d}_{gp}, \quad \frac{\partial \alpha_{gp}}{\partial \mathbf{d}_{gp}} = o_g \exp(e_{gp}) (-\Sigma_g^{-1} \mathbf{d}_{gp})$$

Then,

$$\frac{\partial L}{\partial \mathbf{d}_{gp}} = \frac{\partial L}{\partial I_p} I_g \frac{\partial \alpha_{gp}}{\partial \mathbf{d}_{gp}} = -I_g \frac{\partial L}{\partial I_p} o_g \exp(e_{gp}) \Sigma_g^{-1} \mathbf{d}_{gp}$$

Using  $\mathbf{d}_{gp} = \mathbf{c}_p - \mu_g$ , we get:

$$\frac{\partial L}{\partial \mu_g} = -\sum_p \frac{\partial L}{\partial \mathbf{d}_{gp}}, \quad \frac{\partial L}{\partial \mathbf{c}_p} = \sum_g \frac{\partial L}{\partial \mathbf{d}_{gp}}$$

5) *Gradient w.r.t. Covariance  $\Sigma_g$* : From:

$$e_{gp} = -\frac{1}{2} \mathbf{d}_{gp}^\top \Sigma_g^{-1} \mathbf{d}_{gp},$$

we use the identity:

$$\frac{\partial e_{gp}}{\partial \Sigma_g} = \frac{1}{2} \Sigma_g^{-1} \mathbf{d}_{gp} \mathbf{d}_{gp}^\top \Sigma_g^{-1}$$

Combining with the chain rule:

$$\begin{aligned}\frac{\partial L}{\partial e_{gp}} &= I_g \frac{\partial L}{\partial I_p} o_g \exp(e_{gp}) \\ \Rightarrow \frac{\partial L}{\partial \Sigma_g} &= \sum_p \frac{\partial L}{\partial e_{gp}} \frac{\partial e_{gp}}{\partial \Sigma_g} \\ &= \frac{1}{2} \sum_p I_g \frac{\partial L}{\partial I_p} o_g \exp(e_{gp}) \Sigma_g^{-1} \mathbf{d}_{gp} \mathbf{d}_{gp}^\top \Sigma_g^{-1}\end{aligned}$$

For covariance vector representation, we store only six unique elements:

$$\text{cov3D}_g = [\sigma_0, \sigma_1, \sigma_2, \sigma_3, \sigma_4, \sigma_5] \Rightarrow \Sigma_g = \begin{bmatrix} \sigma_0 & \sigma_1 & \sigma_2 \\ \sigma_1 & \sigma_3 & \sigma_4 \\ \sigma_2 & \sigma_4 & \sigma_5 \end{bmatrix}$$

To compute  $\frac{\partial L}{\partial \sigma_i}$ , we symmetrize the gradient:

$$\frac{\partial L}{\partial \sigma_i} = \begin{cases} (\frac{\partial L}{\partial \Sigma_g})_{ii} & \text{for diagonal } \sigma_i \\ \frac{1}{2} \left[ (\frac{\partial L}{\partial \Sigma_g})_{cd} + (\frac{\partial L}{\partial \Sigma_g})_{dc} \right] & \text{for off-diagonal } (c, d) \end{cases}$$

6) *Propagation to Scale and Rotation*: We use:

$$\begin{aligned}\Sigma_g &= M_g^\top M_g, \quad M_g = S_g R_g \\ \Rightarrow \frac{\partial L}{\partial M_g} &= 2M_g \frac{\partial L}{\partial \Sigma_g}, \quad \frac{\partial L}{\partial S_g} = \frac{\partial L}{\partial M_g} R_g, \quad \frac{\partial L}{\partial R_g} = \frac{\partial L}{\partial M_g} S_g\end{aligned}$$

7) *Gradient w.r.t. Quaternion  $q_g$* : We represent rotation using quaternions  $q_g = [q_r, q_i, q_j, q_k]$ . The corresponding rotation matrix  $R(q_g)$  is defined analytically. To differentiate, we compute:

$$\frac{\partial L}{\partial q_m} = \sum_{u,v} \frac{\partial L}{\partial [R_g]_{uv}} \frac{\partial [R(q_g)]_{uv}}{\partial q_m}, \quad m \in \{r, i, j, k\}$$

To backpropagate through quaternion normalization  $q_g = \tilde{q}_g / \|\tilde{q}_g\|$ , we use:

$$\frac{\partial L}{\partial \tilde{q}_g} = \frac{1}{\|\tilde{q}_g\|} (I - q_g q_g^\top) \frac{\partial L}{\partial q_g}$$

## B. Initialization Schemes

We define the two initialization strategies used for setting Gaussian means  $\mu_g$ :

1) *On-slice initialization*: Assuming a known slice pose with rotation  $R_S \in \mathbb{R}^{3 \times 3}$  and translation  $\mathbf{t}_S \in \mathbb{R}^3$ , we define a 2D reference grid:

$$\mathcal{P} = \{(x_i, y_j, 0) \in \mathbb{R}^3 \mid x_i \in [a_x, b_x], y_j \in [a_y, b_y]\}$$

with uniform grid spacing. The 3D Gaussian centers are then computed via:

$$\mu_{ij} = R_S(p_{ij} + \mathbf{t}_S), \quad p_{ij} \in \mathcal{P}$$

2) *Uniform sampling*: If no pose is known, we sample:

$$\mu_g = \mathbf{a} + (\mathbf{b} - \mathbf{a}) \odot \xi_g, \quad \xi_g \sim \mathcal{U}[0, 1]^3$$

where  $\mathbf{a}, \mathbf{b} \in \mathbb{R}^3$  define the bounding box.

A visual comparison of these two initialization strategies is shown in Fig. 16. On-slice initialization produces structured, well-aligned Gaussians from the start, whereas uniform sampling yields a diffuse cloud of Gaussians that must be refined during training.

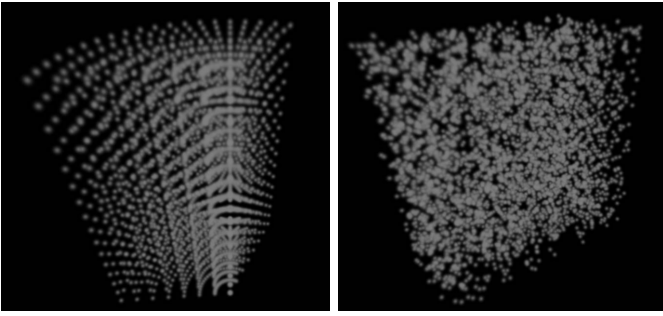


Fig. 16. Left: On-Slice initialization for a sagittal sweep. Right: Random initialization for a sagittal sweep.

### C. Inactive Gaussians and Density Control

Our density control mechanism involves periodic pruning and reinitialization of Gaussians based on their contribution metric  $m_g = |I_g \cdot o_g|$ . Below are the key implementation details:

1) *Pruning Schedule.*: Every 10 epochs, we evaluate all Gaussians and mark those with:

$$m_g = |I_g \cdot o_g| < \epsilon, \quad \text{with } \epsilon = 10^{-4}$$

as inactive. These are removed from the parameter set.

2) *Reinitialization.*: For each removed Gaussian, a new one is inserted. The new mean  $\mu_g$  is sampled uniformly within the current bounding box of active Gaussian means:

$$\mu_g \sim \mathcal{U}[\mu_{\min}, \mu_{\max}]$$

All other parameters are initialized using the defaults described in Section IV-D.

3) *Optional Filters.*: To prevent rapid re-deactivation, newly inserted Gaussians can be given a brief "grace period" (e.g., skipped in the next one or two pruning steps). This lightweight mechanism stabilizes training and improves efficiency, particularly in early epochs where many Gaussians otherwise become stuck.

Tables VI and VII show the search results for the alternative method proposed for inactive Gaussians.

TABLE VI

L1 AND SSIM METRICS ON DIFFERENT LEARNING RATES FOR MEANS

Metric	0.15		0.2		0.25	
	L1	SSIM	L1	SSIM	L1	SSIM
Means	0.0201	0.8642	<b>0.0189</b>	0.8692	0.201	<b>0.8700</b>

TABLE VII

L1 AND SSIM METRICS ON DIFFERENT LEARNING RATES

Metric	0.005		0.01		0.05	
	L1	SSIM	L1	SSIM	L1	SSIM
Opacities	0.0228	0.8451	<b>0.0213</b>	0.8485	0.0221	<b>0.8518</b>
Scales	0.0171	0.8671	<b>0.0169</b>	<b>0.8680</b>	0.0221	0.8518
Intensities	<b>0.0194</b>	0.8540	0.0195	<b>0.8546</b>	0.0221	0.8518

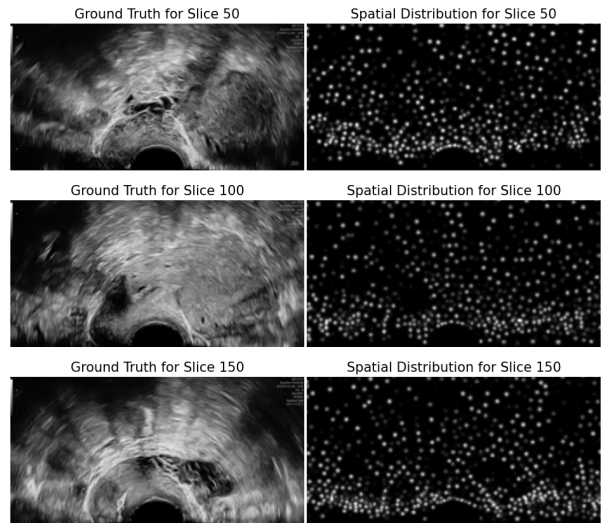


Fig. 17. Distribution of Gaussian primitives for a scene.

### D. Spatial convergence

Fig. 17 visualizes the spatial distribution of Gaussians after optimization. For clarity, all opacities and intensities are set to 1.0, and Gaussian scales are reduced by a factor of 0.2. The visualizations show that Gaussians concentrate in high-intensity areas corresponding to meaningful anatomical structures, while low-intensity regions remain largely empty—reflecting the model’s ability to focus its representational capacity where it matters most.

Fig. 18 illustrates how Gaussian centers evolve during training, comparing a sparse configuration ( $\approx 24$  Gaussians per slice) to a denser one ( $\approx 112$  per slice). With fewer Gaussians, individual movements are larger and more distinct, as each primitive covers more space. In denser settings, movement is subtler due to increased redundancy.

Notably, Gaussians exhibit dynamic reallocation: some exit the visualized slice while others enter or converge toward high-intensity regions. This behavior suggests an adaptive mechanism that reallocates primitives toward regions of higher relevance or deactivates them when unnecessary, enabling efficient use of limited representational resources.

### E. Implementation Optimizations

Efficient training of the differentiable rasterizer requires high-performance implementation of both the forward and backward passes due to the dense, per-pixel evaluation of contributions from thousands of 3D Gaussians. This section describes the key CUDA-level optimizations applied to ensure computational feasibility and scalability.

1) *Precomputation of Reusable Quantities.*: The backward pass relies heavily on values such as  $\Sigma_g^{-1}$ , which are reused across all pixels influenced by a given Gaussian. To avoid redundant computation, we launch a dedicated kernel that precomputes  $\Sigma_g^{-1}$  for all Gaussians and stores the upper-triangular components in a compact 6-element representation. These cached inverses are then accessed during both forward and backward passes to evaluate  $e_{gp}$ ,  $\alpha_{gp}$ , and their gradients.

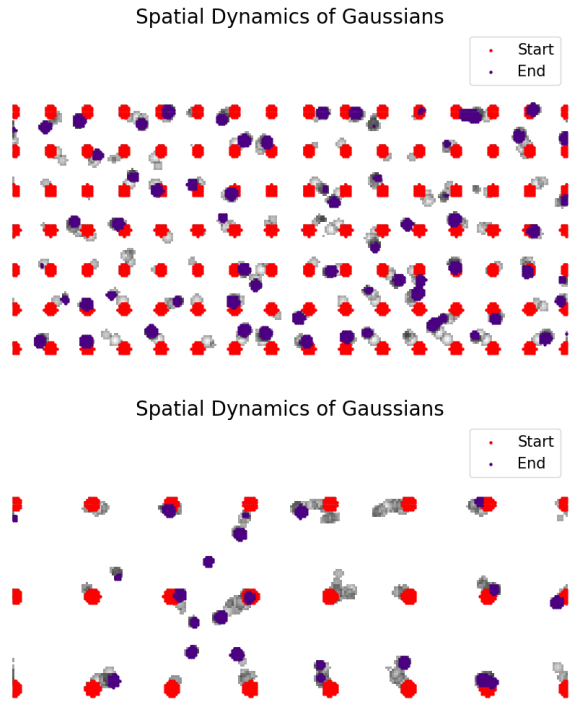


Fig. 18. Trajectory of Gaussian centers during training for the same slice, comparing different quantities of Gaussians. Grey traces indicate movement paths. Some Gaussians appear only at the start or end of the trajectory within the slice, suggesting they originated from or moved to adjacent slices.

Similarly, we precompute  $\Sigma_g^{-1}\mathbf{d}_{gp}$  wherever possible to avoid recomputation during the accumulation of gradient terms. This significantly reduces arithmetic overhead in the main rasterization kernels.

2) *Shared Memory Tiling*: A major bottleneck in GPU rasterization is the repeated access to Gaussian parameters from global memory. To mitigate this, we divide the set of Gaussians into tiles of size  $T$  (e.g., 64). Each CUDA thread block loads one tile of Gaussian data (means, scales, quaternions, opacities, intensities) into shared memory. Threads within the block synchronize and reuse the shared memory tile for computing contributions and gradients for their assigned pixels. This results in reduction in global memory bandwidth usage, better memory coalescing and cache locality and increased parallel efficiency and occupancy.

3) *Symmetric Covariance Storage and Update*: Each 3D Gaussian covariance matrix  $\Sigma_g$  is symmetric. During the backward pass, we compute  $\frac{\partial L}{\partial \Sigma_g}$  as a full matrix. Each symmetric entry (e.g.,  $\sigma_1$ , appearing in both  $(0, 1)$  and  $(1, 0)$ ) receives contributions from both locations and is updated using their average. This saves memory, reduces write operations, and simplifies gradient accumulation logic.

4) *Matrix-Free Operations*: To minimize expensive matrix multiplications and inversions, we unroll expressions like  $\mathbf{d}_{gp}^T \Sigma_g^{-1} \mathbf{d}_{gp}$  into explicit component-wise dot products using precomputed inverse covariances. Gradients involving matrix-vector products are similarly computed via direct arith-



Fig. 19. Effect of cumulative optimization strategies on training time.

metic to avoid launching linear algebra kernels. This low-level optimization is especially effective for backward steps where every saved FLOP improves scalability.

5) *Compiler-Level Optimizations*: To further improve performance, we apply the following compiler flags during kernel compilation

- `-O3`: Enables aggressive optimizations like loop unrolling, constant folding, and function inlining.
- `--use_fast_math`: Activates fast approximations for transcendental functions (e.g., `exp`, `sqrt`), which are sufficient for training purposes and significantly faster.

In practice, these flags reduce kernel runtime by 20–40% without compromising training stability.

6) *Quantitative Impact*: Fig. 19 shows the training time required to fit a fixed US volume as each optimization is introduced cumulatively. The baseline PyTorch implementation (no tiling, no precomputation, no matrix unrolling) takes approximately 18 hours. Our optimized CUDA implementation reduces this to under 2 hours for a scene with over 50,000 Gaussians.